Science of the Total Environment 891 (2023) 164404

Contents lists available at ScienceDirect

Science of the Total Environment

journal homepage: www.elsevier.com/locate/scitotenv

Isotopic investigation of sources and processes affecting gaseous and particulate bound mercury in the east coast, South Korea

Hoin Lee [a], Sae Yun Kwon [a,*], Jonghun Kam [a], Kitack Lee [a], Xuewu Fu [b], In-Gyu Cho [c], Sung-Deuk Choi [c]

[a] Division of Environmental Science and Engineering, Pohang University of Science and Technology, Pohang 37673, South Korea
[b] State Key Laboratory of Environmental Geochemistry, Institute of Geochemistry, Chinese Academy of Sciences, Guiyang 550081, China
[c] Department of Urban and Environmental Engineering, Ulsan National Institute of Science and Technology, Ulsan 44919, South Korea

HIGHLIGHTS

- Both anthropogenic and natural Hg emissions are prevalent in East Asia.
- Hg stable isotopes and HYSPLIT are used to identify potential Hg sources.
- TGM is mainly sourced from coastal surface evasion and long-range transport.
- PBM is emitted from local anthropogenic activities and processed photochemically.
- Our PBM represents a regional isotopic end-member across East Asia.

GRAPHICAL ABSTRACT

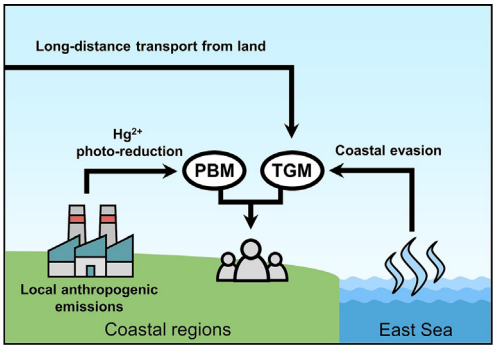

ARTICLE INFO

Editor: Mae Sexauer Gustin

Keywords:
Mercury
Stable isotope
Coastal
East Asia
Total gaseous mercury (TGM)
Particulate bound mercury (PBM)

ABSTRACT

Understanding sources and processes affecting atmospheric mercury (Hg) are key to enabling targeted Hg managements under the Minamata Convention on Mercury. We employed stable isotopes (δ^{202}Hg, Δ^{199}Hg, Δ^{201}Hg, Δ^{200}Hg, Δ^{204}Hg) and backward air trajectories to characterize sources and processes affecting total gaseous Hg (TGM) and particulate bound Hg (PBM) in a coastal city, South Korea, subjected to atmospheric Hg sources of a local steel manufacturing industry, coastal evasion from the East Sea, and long-distance transport from East Asian countries. Based on the simulated airmasses and the isotopic comparison with TGM characterized from other urban, remote, and coastal sites, TGM evaded from the coastal surface of the East Sea (warm seasons) and from the land surface in high latitude regions (cold seasons) act as important sources relative to local anthropogenic emissions at our study location. Conversely, a significant relationship between Δ^{199}Hg and concentrations of PBM ($r^2 = 0.39$, $p < 0.05$) and a seasonally uniform Δ^{199}Hg/Δ^{201}Hg slope (1.15), except for summer (0.26), suggest that PBM is generally sourced from local anthropogenic emissions and subjected to Hg^{2+} photo-reduction on particles. The striking isotopic similarity between our PBM (δ^{202}Hg; −0.86 to 0.49 ‰, Δ^{199}Hg; −0.15 to 1.10 ‰) and those previously characterized along the coastal and offshore regions of the Northwest Pacific (δ^{202}Hg; −0.78 to 1.1 ‰, Δ^{199}Hg; −0.22 to 0.47 ‰) infer that anthropogenically emitted PBM from East Asia and those processed in the coastal atmosphere serves as a regional isotopic end-member. The implementation of air pollution control devices can reduce local PBM, while regional and/or multilateral efforts are required to manage TGM evasion and transport. We also anticipate that the regional isotopic end-member can be used to quantify the relative influence of local anthropogenic Hg emissions and complex processes affecting PBM in East Asia and other coastal regions.

* Corresponding author.
E-mail address: saeyunk@postech.ac.kr (S.Y. Kwon).

http://dx.doi.org/10.1016/j.scitotenv.2023.164404
Received 16 March 2023; Received in revised form 16 May 2023; Accepted 20 May 2023
Available online 26 May 2023

1. Introduction

Mercury (Hg) is a globally distributed atmospheric pollutant, which can cause negative ecosystem and human health impacts upon exposure (Driscoll et al., 2013; Mergler et al., 2007). The processes leading to atmospheric Hg deposition and subsequent accumulation in the biosphere are largely dependent on redox transformations between operationally defined Hg species (Amos et al., 2012). Gaseous elemental Hg (GEM or Hg^0) occupies the largest atmospheric Hg fraction (~90 %) and travels long distances from the source region of primary anthropogenic emission and secondary re-emission from geochemical surfaces (Selin, 2009). Upon oxidation or binding with particles, gaseous oxidized Hg (GOM or Hg^{2+}) and particulate bound Hg (PBM) deposit rapidly to the biosphere in the form of wet and dry deposition. Among the operationally defined species, Hg^0 and PBM are regarded to be important media for evaluating the effectiveness of the Minamata Convention (MC), a multilateral agreement to mitigate anthropogenic Hg emissions (Kwon et al., 2020). This is because PBM is generally sourced from local anthropogenic emissions and can account for >40 % in industrial regions (Guo et al., 2022), and Hg^0 reflects globally distributed Hg species. From the policy perspective, quantifying temporal changes in Hg^0 and PBM can inform the effectiveness of both local and global policies and technologies implemented under the MC.

Quantifying Hg concentration alone has been challenged by the recent scientific debate regarding potential sources and/or processes governing temporal trends in atmospheric Hg species (Kwon and Selin, 2016). More specifically, while much of the concentration measurements report noticeable reductions in atmospheric Hg species over the Northern Hemisphere in recent decades (Butler et al., 2008; Cole et al., 2013; Slemr et al., 2011), conflicting hypotheses, including a reduction in anthropogenic emission, legacy Hg, and re-emission from the ocean surface, have been proposed to explain the observed changes (Soerensen et al., 2012; Zhang et al., 2016). As for the PBM, simulations of a global Hg model suggest that Hg^0 oxidation followed by gas-phase particle adsorption plays an equally important role in explaining the measured PBM in addition to direct anthropogenic emissions (Amos et al., 2012). We propose that targeted Hg management, especially under the MC, is dependent on the insights of specific sources and processes affecting atmospheric Hg species over time and space.

Here, we employ Hg stable isotopes to characterize sources and processes affecting Hg^0 and PBM in a coastal city of South Korea. Mercury isotopes have proven useful for identifying the influence of various anthropogenic and natural Hg sources (e.g., Blum et al., 2014; Kwon et al., 2020). Mass-dependent (MDF; $\delta^{202}Hg$) and mass-independent fractionation (MIF; $\Delta^{199}Hg$, $\Delta^{201}Hg$, $\Delta^{200}Hg$, $\Delta^{204}Hg$) of Hg isotopes have also provided insights into biogeochemical processes modifying Hg sources, transport, and fate (Sonke, 2011; R. Sun et al., 2019). MIF of the even- ($\Delta^{200}Hg$, $\Delta^{204}Hg$) and odd-mass number isotopes ($\Delta^{199}Hg$, $\Delta^{201}Hg$) are regarded to be particularly beneficial to the understanding of atmospheric processes. This is because $\Delta^{200}Hg$ and $\Delta^{204}Hg$ changes occur primarily via Hg^0 photo-oxidation in the high troposphere and photodissociation of Hg-oxides (Cai and Chen, 2016; Sun et al., 2022). As for $\Delta^{199}Hg$ and $\Delta^{201}Hg$, Hg^{2+} photo-reduction and methylmercury (MeHg) photo-degradation are the primary processes resulting in measurable $\Delta^{199}Hg$ changes in both aqueous solution (Bergquist and Blum, 2007) and in aerosols with high moisture content (Huang et al., 2021).

Unlike the past isotopic characterizations of Hg^0 and PBM in inland urban and remote sites (Das et al., 2016; Guo et al., 2022; Huang et al., 2016, 2018; Xu et al., 2017), recent atmospheric monitoring over coastal and offshore regions of the Northwest Pacific are shedding light into the regional influence of anthropogenic Hg emissions in East Asia and complex processes (i.e., photo-reduction, photo-oxidation, oxidation followed by particle adsorption) dictating Hg^0 and PBM isotope ratios in the coastal atmosphere (Fu et al., 2018; Huang et al., 2022; Qiu et al., 2021; Xu et al., 2021). Moreover, controlled experiments in gas- and aqueous phases reveal that physicochemical properties of PBM can overwhelm the effect of source isotopic signatures by inducing unique redox chemistry (Huang et al., 2021; Zhang et al., 2022; Zhao et al., 2021).

Building upon the recent and emerging studies across coastal regions of East Asia and the Northwest Pacific (Fu et al., 2018; Huang et al., 2022; Qiu et al., 2021; Xu et al., 2021), we aim to characterize sources and processes affecting Hg^0 and PBM in a coastal city of Pohang, South Korea. We hypothesize that Pohang is influenced by both local anthropogenic Hg emissions and regional Hg supplied by East Asia and the Northwest Pacific, with their contributions varying temporally by seasonal airmasses and by different atmospheric Hg species. There is a presence of the world's fifth-largest steel manufacturing industry, known to emit substantial amounts of Hg and other atmospheric pollutants (e.g., SO_2, NOx, PM) (Streets et al., 2017, 2019; Tang et al., 2020). Pohang is also situated on the East Sea of the Northwest Pacific and receive airmass transport from the east coast and inland north, including China (Shin et al., 2020; Zhu et al., 2022), which accounts for the largest fraction of the global anthropogenic Hg emission (Streets et al., 2019; UNEP, 2019). The results of this study would enable targeted local Hg managements under the MC and generate a regional atmospheric Hg isotopic end-member reflecting inland and/or coastal influences of East Asia.

2. Materials and methods

2.1. Site description

Pohang is located on the southeast coast of South Korea and our sampling station is located ~5 km away from the East Sea (Fig. 1). Pohang is a suburban city with an area of 1129 km^2 and a population of ~500,000. A key industrial feature of Pohang is the operation of the world's fifth-largest steel manufacturing industry, known to emit substantial amounts of Hg and other atmospheric pollutants (e.g., SO_2, NOx, PM) (Streets et al., 2017, 2019; Tang et al., 2020). Prior characterizations of TGM across South Korean cities have reported a slightly higher concentration of ~5.0 ng/m^3 at Pohang relative to other urban cities (2.1–3.7 ng/m^3, Seo et al., 2016). Surrounding the steel manufacturing industry are ~300 small-scale industries, which manufacture steel, electrical equipment, chemicals, and non-ferrous metals. Based on the analyses conducted by the Pohang Environmental Policy Division in 2017 and by Jung et al. (2021), the total Hg (THg) levels in both sludge and wastewater collected from 160 facilities were lower than the domestic Hg loading limit of 5 μg/L, indicating that they release small amounts of Hg into the local environment.

To assess the overall anthropogenic influence of the steel manufacturing industry, we collected total gaseous Hg (TGM; GEM + GOM), PBM, and Fe aerosols (both in the form of total suspended particles; TSP) on the rooftop of a library building (10 m above ground) at Pohang University of Science and Technology (POSTECH). Substantial Fe emissions are thought to occur in the form of aerosols from the steel manufacturing industries (Baek et al., 2020; Hleis et al., 2013). Additional anthropogenic emission indicators of $PM_{2.5}$, PM_{10}, and various oxidants for Hg (O_3, NO_2, CO, SO_2) were obtained from the national air quality monitoring system (AirKorea, https: //www.airkorea.or.kr/) (Table A.1.), located 4 km away from our sampling station (Fig. 1, Fig. A.1.).

2.2. Sample collection

All atmospheric samples of TGM, PBM and Fe aerosols were collected for a total of five periods involving all four seasons spanning winter (January), spring (April), summer (August) and autumn (November) of 2021, and spring (March) of 2022. Individual days of sampling periods and the associated meteorological and environmental parameters, obtained from the Automated Synoptic Observation System (ASOS) (Korea Meteorological Administration Weather Data Service, https://data.kma.go.kr/) and the national air quality monitoring system, are shown in Table A.1.

The TGM was collected onto a gold trap via an air sampling pump (Flite3, SKC) at a flow rate of 1.84 L/min. A PTFE filter (0.45 μm, 25 mm) and soda trap were connected in front of a gold trap to remove moisture and particles from entering the trap. Prior to sampling, all gold

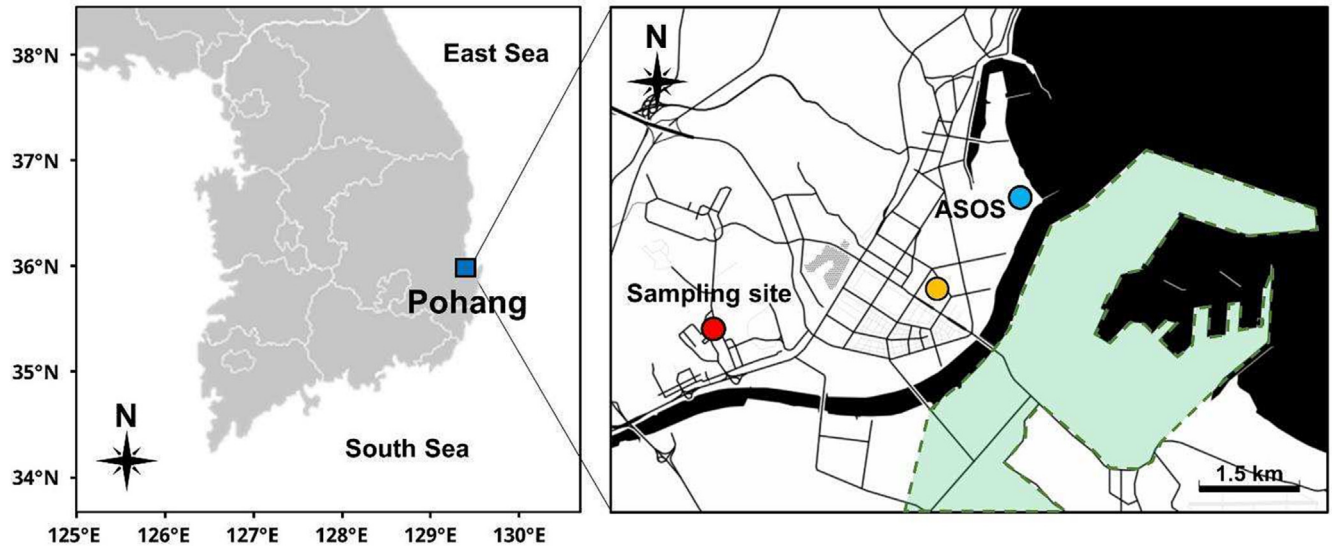

Fig. 1. A map showing the locations of sampling site (red circle), air quality monitoring station (AirKorea, yellow circle), automated synoptic observation system (ASOS, blue circle), and steel manufacturing industry (green area) in Pohang, South Korea.

traps were desorbed at 600 °C to remove residual Hg. Sampling of TGM was conducted for 10 h per day and for three days per season. The PBM was characterized by sampling TSP via a high-volume air sampler (HiVol, HV-1000R, Sibata, Japan) at a flow rate of 1000 L/min using a quartz fiber filter (QR-100, 203 × 254 mm, Advantec, Japan). PBM was sampled for 23 h per day and for five to nine days per season. Prior to sampling, all quartz fiber filters were baked at 450 °C for 3 h and particle weights were measured using an analytical balance (ME204, Mettler Toledo, Singapore).

Concentrations of Fe were characterized in TSP with particle sizes >0.49 μm. We refer to them as Fe aerosols here after. Fe aerosols were sampled via a HiVol (HV-1000R, Sibata, Japan) at a flow rate of 1132 L/min using a PTFE filter (TE-230-PTFE, Tisch Environmental Inc., U.S.). Fe aerosols were sampled for 23 h per day and for 10–13 days per season. Prior to sampling, all PTFE and background filters (PF050, 203 × 254 mm, Advantec, Japan) were washed with 3 mol/L HNO_3, 3 mol/L HCl, and ultrapure water (Kurisu et al., 2019; Sakata et al., 2018) and weighed using an analytical balance. After sampling for PBM and Fe aerosols, filters were sealed in a polyethylene bag and stored at −20 °C (freezer) and a vacuum desiccator, respectively.

2.3. Analysis

2.3.1. Hg and Fe concentrations

The TGM captured onto a gold trap was desorbed at 600 °C. The PBM collected on a quartz filter was freeze-dried and combusted via a dual-stage thermal combustion furnace. Both TGM and PBM were released in the form of Hg^0, which were preconcentrated into an individual 1 % $KMnO_4$ (in 10 % H_2SO_4) solution. A cold vapor atomic fluorescence spectroscopy (CV-AFS, Brooks Rand, U.S.) was used to measure THg concentration. The average recovery of the standard reference material NIST 2711a (Montana II soil) was 88 ± 16 % (n = 4). The field blank filters had <5 % of THg collected on quartz fiber filters.

Filters containing Fe aerosols were soaked in 15.2 mol/L HNO_3 and evaporated at 120 °C to dryness. The solution was diluted with ultra-pure water at 0.3 mol/L HNO_3 and filtered using a 0.2 μm PTFE syringe filter (Kurisu et al., 2019). Fe concentration in solution was analyzed using an inductively coupled plasma optical emission spectrometer (ICP-OES, Thermo Scientific iCAP 6300). The average recovery of the standard reference material TORT-3 (lobster) was 98 ± 6 % (n = 31). Field blank filters had <1 % of the total Fe collected on PTFE filters. Seasonal Fe concentrations and detection limits are found in Table A.3.

2.3.2. Hg isotopes

The 1 % $KMnO_4$ solutions containing PBM and TGM were introduced into a multicollector inductively coupled plasma mass spectrometer (MC-ICP-MS, Nu Instruments III, U.K.) by continuously reducing Hg^{2+} with 2 % $SnCl_2$ and by separating Hg^0 using a glass gas-liquid phase separator. Instrumental mass bias was corrected using an internal Tl standard (NIST 997), which was introduced via desolvating nebulizer (Aridus 3, CETAC, U.S.) and by bracketing each sample with NIST SRM 3133 matched to the sample matrix. MDF is reported as $\delta^{202}Hg$ in permil (‰) relative to NIST SRM 3133.

$$\delta^{202}Hg = \left\{ \left[\left({}^{202}Hg/{}^{198}Hg\right)_{sample} / \left({}^{202}Hg/{}^{198}Hg\right)_{NIST3133} \right] - 1 \right\} \times 1000 \quad (1)$$

MIF is reported as $\Delta^{199}Hg$, $\Delta^{200}Hg$, $\Delta^{201}Hg$, and $\Delta^{204}Hg$ (‰) and was calculated using the following equations (Bergquist and Blum, 2007).

$$\Delta^{199}Hg\ (‰) = \delta^{199}Hg - \left(\delta^{202}Hg \times 0.2520\right) \quad (2)$$

$$\Delta^{200}Hg\ (‰) = \delta^{200}Hg - \left(\delta^{202}Hg \times 0.5024\right) \quad (3)$$

$$\Delta^{201}Hg\ (‰) = \delta^{201}Hg - \left(\delta^{202}Hg \times 0.7520\right) \quad (4)$$

$$\Delta^{204}Hg\ (‰) = \delta^{204}Hg - \left(\delta^{204}Hg \times 1.4930\right) \quad (5)$$

Analytical uncertainty of 2SD was estimated based on the replicate analysis of NIST 2711a (n = 4). The Hg isotope ratios of NIST 2711a and NIST RM 8610 from this study and those obtained from prior studies are reported in Table A.2.

2.3.3. Backward air trajectory

The Hybrid Single Particle Lagrangian Integrate Trajectory (HYSPLIT) model developed by the National Ocean and Atmospheric Administration (NOAA) was used (Draxler and Hess, 1998) to simulate airmasses arriving at the sampling site. The HYSPLIT was operated with gridded meteorological data from the Global Data Assimilation System (GDAS) and 72-hour backward air trajectories were calculated starting at 13 KST (04 UTC) at daily intervals spanning our sampling period. In the model setting, the starting height of trajectories was set to 500 m above ground, where air pollutants are well mixed within the atmospheric boundary layer. Wind rose diagrams were drawn for comparison by using the wind direction

and wind frequency information obtained from the Automated Synoptic Observation System (ASOS). As illustrated in Fig. A.1., the northeast side of the ASOS is facing the East Sea (coastal influence) and the southwest side of the ASOS is facing the inland.

3. Results and discussion

3.1. Regional comparison of PBM and TGM

The PBM and TGM concentrations range between 2.5 and 326 pg/m^3 (74.5 ± 76.3 pg/m^3; n = 38) and between 0.87 and 4.2 ng/m^3 (1.90 ± 0.83 ng/m^3; n = 16), respectively (Table A.3.). The observed concentrations are, on average, lower than those measured at urban sites (PBM; 191 to 640 pg/m^3, TGM; 2.3 to 7.9 ng/m^3) but higher relative to remote sites of China and India (PBM; 25 to 84 pg/m^3, TGM; 1.2 to 2.5 ng/m^3) (Qiu et al., 2021; Shi et al., 2022). In regards to the seasonal variation, we observed minor seasonal fluctuations in both PBM (spring 21; 40 ± 33 pg/m^3, n = 7, summer 21; 52 ± 52 pg/m^3, n = 9, autumn 21; 92 ± 91 pg/m^3, n = 9, winter 21; 87 ± 98 pg/m^3, n = 4, spring 22; 103 ± 95 pg/m^3, n = 9) and TGM concentrations (spring 21; 2.3 ± 1.0 ng/m^3, n = 3, summer 21; 2.0 ± 0.15 ng/m^3, n = 3, autumn 21; 2.7 ± 1.3 ng/m^3, n = 3, winter 21; 1.3 ± 0.21 ng/m^3, n = 3, spring 22; 1.4 ± 0.37 ng/m^3, n = 4). This may be owing to the small dataset representing the individual season. Within individual season, there are large daily variations in the PBM and more uniform TGM concentrations throughout the sampling period.

Despite the minor seasonal trend in TGM concentrations, the isotope ratios of TGM exhibit a wide δ^{202}Hg (−2.46 to 0.06 ‰, mean; −1.02 ± 0.79 ‰, n = 16) and a small Δ^{199}Hg range (−0.24 to 0.02 ‰, mean; −0.09 ± 0.08 ‰) with relatively distinct seasonal δ^{202}Hg (Fig. 2A). The PBM show a small δ^{202}Hg (−0.86 to 0.49 ‰, mean; −0.12 ± 0.34 ‰, n = 36) and a wide Δ^{199}Hg range (−0.15 to 1.10 ‰, mean; 0.12 ± 0.25 ‰) with minor seasonal differences (Fig. 2B). In regards to Δ^{200}Hg, we observe overall positive values in the PBM (0.00 to 0.10 ‰, mean; 0.04 ± 0.03 ‰) and near-zero to negative values in the TGM (−0.11 to 0.02 ‰, mean; −0.03 ± 0.03 ‰) (Table A.3.). This is consistent with prior studies, which suggested that measurable Δ^{200}Hg changes occur only via Hg^0 photo-oxidation and photo-dissociation of Hg-oxides, both of which cause Hg^{2+} with a higher Δ^{200}Hg relative to Hg^0 (Cai and Chen, 2016; Sun et al., 2022).

Given the absence of Hg isotope data in atmospheric samples of South Korea, we compare our results with TGM and PBM sampled at various locations of the U.S., China and in the Northwest Pacific (Demers et al., 2013; Fu et al., 2018, 2019; Gratz et al., 2010; Huang et al., 2015, 2016, 2019, 2022; Li et al., 2020; Qiu et al., 2022; Rolison et al., 2013; Sherman et al., 2010; Xu et al., 2017, 2021; Yu et al., 2016). As illustrated in Fig. 2A, the isotope ratios of our TGM collected in autumn and winter are within the ranges of TGM characterized at urban and remote sites of inland China (Demers et al., 2013; Gratz et al., 2010; Sherman et al., 2010; Xu et al., 2017; Yu et al., 2016). The TGM sampled in spring and summer are within the ranges of those measured at urban sites (Xu et al., 2017; Yu et al., 2016) and TGM known to be transported from coastal regions (Rolison et al., 2013). The TGM of spring 22 have a wide range in δ^{202}Hg, spanning across various sources. As for the PBM, we observe overall positive δ^{202}Hg and Δ^{199}Hg relative to PBM characterized at remote and urban sites of China (Fig. 2B) (Fu et al., 2019; Huang et al., 2015, 2016, 2019; Rolison et al., 2013; Xu et al., 2017; Yu et al., 2016). Interestingly, the isotope ratios of our PBM are more similar to those collected at a coastal city of Daimeishan, China (Xu et al., 2021) and overlap with PBM sampled on cruise along coastal and offshore regions of the Northwest Pacific around East Asia (Huang et al., 2022; Qiu et al., 2021). The low δ^{202}Hg and Δ^{199}Hg have repeatedly been characterized in PBM sampled downstream of point Hg emission sources (Das et al., 2016; Xu et al., 2017; Yu et al., 2016) and were attributed to negative δ^{202}Hg and near-zero Δ^{199}Hg in anthropogenic source materials used during coal combustion (δ^{202}Hg; −1.10 ‰), smelting (δ^{202}Hg; −0.87 ‰), and cement manufacturing processes (δ^{202}Hg; −1.42 ‰) (Huang et al., 2016). Anthropogenically emitted PBM, modeled by R. Sun et al. (2016), also have δ^{202}Hg of −1.17 ‰ and near-zero Δ^{199}Hg. In contrary, the positive δ^{202}Hg and Δ^{199}Hg in PBM along coastal and offshore regions of the Northwest Pacific have been explained by Hg^{2+} photo-reduction bound to particles (Huang et al., 2022; Qiu et al., 2021; Xu et al., 2021).

In summary, the distinct seasonal δ^{202}Hg of TGM suggest that the sources of TGM may vary across season at our sampling location. Conversely, the narrow δ^{202}Hg and wide Δ^{199}Hg range of PBM indicate that the sources of PBM may be relatively uniform. Based on the relatively positive δ^{202}Hg and Δ^{199}Hg, we speculate that our PBM may be subjected to varying extents of Hg^{2+} photo-reduction on particles in the atmosphere. Below we evaluate the sources and processes affecting the two atmospheric Hg species on the east coast of South Korea in detail.

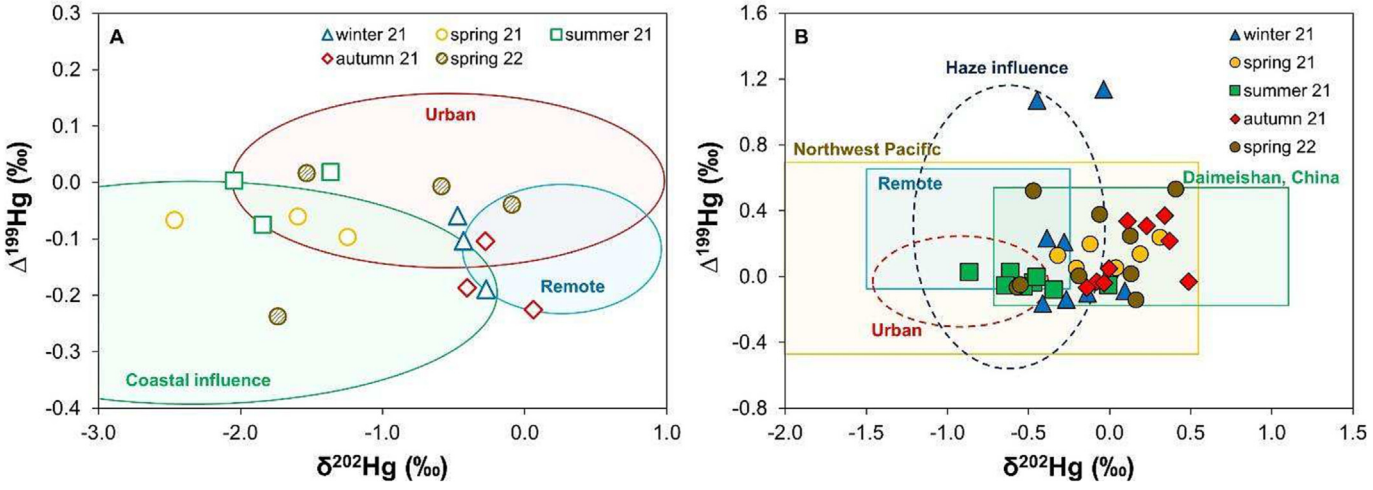

Fig. 2. δ^{202}Hg and Δ^{199}Hg of (A) TGM and (B) PBM. Shaded and dotted areas represent δ^{202}Hg and Δ^{199}Hg ranges of TGM and PBM reported from prior studies at urban (TGM - δ^{202}Hg; −2.03 to 1.11 ‰, Δ^{199}Hg; −0.16 to 0.15 ‰, PBM - δ^{202}Hg; −1.42 to −0.42 ‰, Δ^{199}Hg; −0.31 to 0.19 ‰, Huang et al., 2015, 2016, 2019; Xu et al., 2017, 2019; Yu et al., 2016) and remote sites (TGM - δ^{202}Hg; −0.39 to 0.93 ‰, Δ^{199}Hg; −0.22 to −0.01 ‰, PBM - δ^{202}Hg; −1.45 to −0.26 ‰, Δ^{199}Hg; −0.07 to 0.66 ‰, Demers et al., 2013; Fu et al., 2019; Gratz et al., 2010; Sherman et al., 2010; Yu et al., 2016), and site influenced by coastal evasion (TGM - δ^{202}Hg; −3.88 to −0.33 ‰, Δ^{199}Hg; −0.41 to −0.03 ‰, Northwest Pacific - δ^{202}Hg; −2.53 to 0.57 ‰, Δ^{199}Hg; −0.50 to 0.67 ‰, Daimeishan - δ^{202}Hg; −0.78 to 1.1 ‰, Δ^{199}Hg; −0.22 to 0.47 ‰, Huang et al., 2022; Rolison et al., 2013; Xu et al., 2021) and haze (PBM - δ^{202}Hg; −1.26 to −0.16 ‰, Δ^{199}Hg; −0.62 to 1.14 ‰, Qiu et al., 2022).

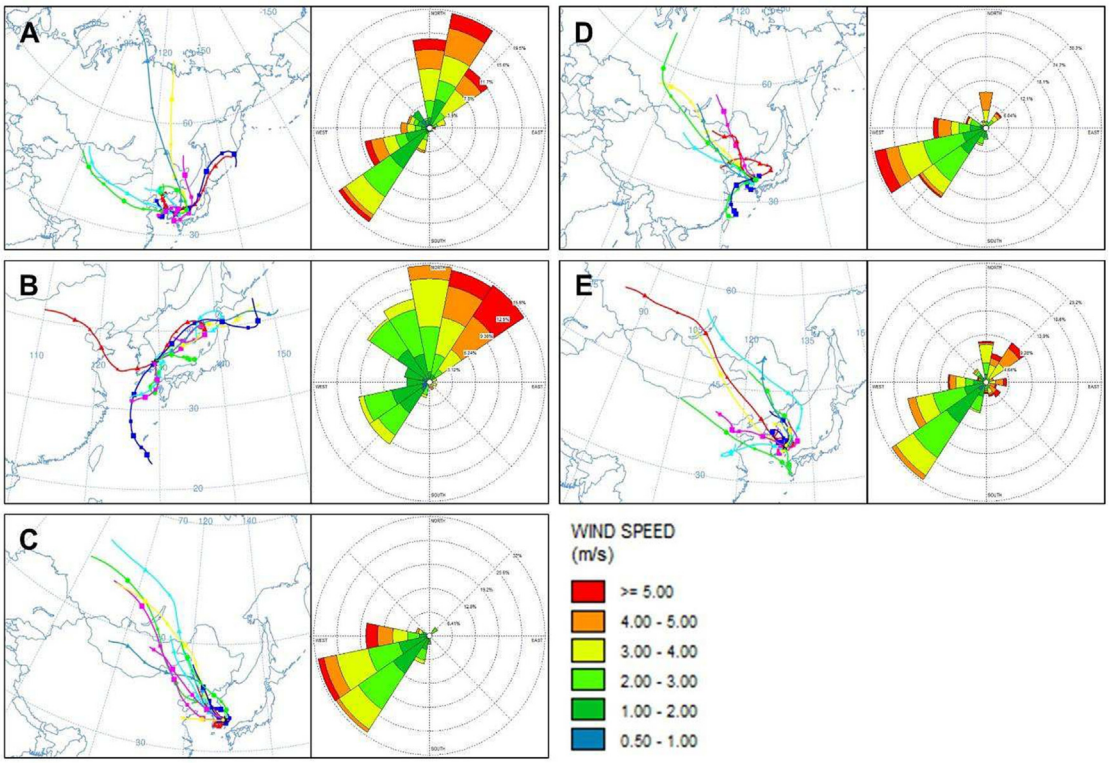

Fig. 3. Backward trajectories (left) and wind roses (right) over five seasons of (A) spring 21, (B) summer 21, (C) autumn 21, (D) winter 21, (E) spring 22. Each line in backward trajectories represents individual sampling day simulated over 72 h of duration. Wind rose shows the wind speed (in color) and the frequency of each wind direction. The northeast side is facing the East Sea and the southwest side is facing inland Pohang as illustrated in Fig. A.1.

3.2. Sources of TGM

There are caveats to interpreting seasonal sources of TGM given our small dataset and minor seasonal variations in TGM concentrations. By employing backward air trajectories and wind roses, we draw insights into potential sources supplying TGM to our study location at least during the periods in which we conducted sampling. The relatively distinct δ^{202}Hg sampled at various seasons together with the absence of a significant relationship between the isotope ratios and concentrations of TGM (in 1/THg; Fig. A.2.) suggest that the sources of TGM may differ across season. Specifically, the δ^{202}Hg of TGM sampled in autumn and winter are within the ranges of TGM characterized at inland urban and remote sites in China (Demers et al., 2013; Gratz et al., 2010; Sherman et al., 2010; Xu et al., 2017; Yu et al., 2016). The δ^{202}Hg of TGM reflecting spring and summer are similar to those measured at urban sites (Xu et al., 2017; Yu et al., 2016) and TGM transported from coastal regions (Rolison et al., 2013). The backward air trajectories and wind roses also display consistently large fractions of airmasses originating from inland and high latitude regions of Russia and China in the cold seasons (autumn, winter) (Fig. 3C, D). The airmass origins are different in the warm seasons (summer, spring) such that there are dominant coastal airmasses in summer (Fig. 3B) and heterogeneous mixtures of inland and coastal airmasses in spring (Fig. 3A, E). The consistency of seasonal airmass origin is well reflected by the δ^{202}Hg variability, with the winter 21 TGM displaying the least amount of δ^{202}Hg variability (1 SD; 0.11 ‰) and the spring 21 and 22 TGM displaying the widest δ^{202}Hg range (1 SD; 0.63–0.78 ‰) (Table A.3.).

Based on the above results, it is possible to interpret TGM sources to mixtures of anthropogenic and background TGM from high latitude regions and TGM evaded from the coastal surface, which may vary in their contributions across season. In addition to δ^{202}Hg, however, Δ^{199}Hg and Δ^{200}Hg have increasingly been utilized to gather insights into sources and relative proportions of Hg^0 and Hg^{2+} in TGM, respectively (Araujo et al., 2022; Demers et al., 2015; Kwon et al., 2020). As mentioned, because only few atmospheric processes result in a higher Δ^{200}Hg in Hg^{2+} relative to Hg^0 (Cai and Chen, 2016; Sun et al., 2022), Δ^{200}Hg has been used to decipher the relative contribution of Hg^0 and Hg^{2+} in natural samples (Araujo et al., 2022; Jiskra et al., 2021; Kwon et al., 2020; Motta et al., 2019). Near-zero to slightly positive Δ^{199}Hg in anthropogenically emitted TGM (reviewed in Kwon et al., 2020) and negative Δ^{199}Hg in background and surface evaded TGM from the coastal surface (Rolison et al., 2013), rice paddy soil (Yin et al., 2013), and snowpack (Araujo et al., 2022) have enabled detailed source tracing.

As illustrated in Fig. 4, we observe generally negative Δ^{199}Hg and Δ^{200}Hg in the cold season TGM, reflecting mixtures of background and surface evaded Hg in the form of Hg^0. The observed Δ^{199}Hg and Δ^{200}Hg together with the effect of high latitude inland airmasses, simulated by the HYSPLIT (Fig. 3C, D), are consistent with the recent evidence suggesting that surface evasion accounts for a large fraction of background TGM over mainland China (Fu et al., 2021). We presume that Hg^0 evaded from the surface over high latitude Russia and China may act as a potential TGM source to our sampling location. Conversely, in the warm seasons, anthropogenically emitted Hg^{2+} with near-zero to slightly positive Δ^{199}Hg and Δ^{200}Hg may be diluted by Hg^0 evaded from the local coastal surface. The effect of dilution is speculated based on coastal airmass transport, simulated by the HYSPLIT (Fig. 3A, B, E), and the relatively uniform TGM concentrations across the warm and cold seasons, indicating that local anthropogenic activities alone are unlikely to be the primary source in the warm seasons. We suggest that Hg^0 evaded from the coastal surface and those evaded and transported from long distances act as important TGM sources relative to local anthropogenic activities in Pohang. The exact seasonal contribution of these TGM sources would require long-term characterization of TGM isotope ratios.

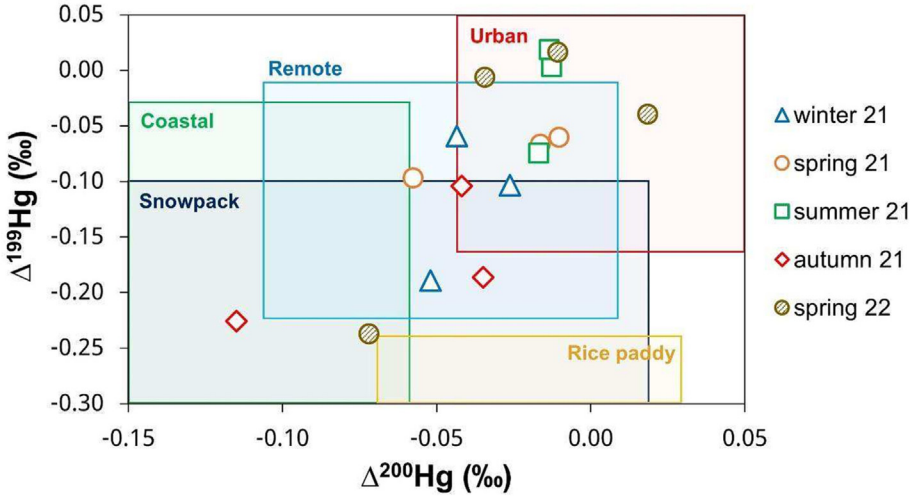

Fig. 4. Δ^{200}Hg and Δ^{199}Hg of the seasonal TGM. Shaded areas represent Δ^{200}Hg and Δ^{199}Hg ranges of TGM reported from prior studies at urban (Δ^{200}Hg; −0.04 to 0.06 ‰, Δ^{199}Hg; −0.16 to 0.15 ‰, Xu et al., 2017; Yu et al., 2016) and remote sites (Δ^{200}Hg; −0.11 to 0.01 ‰, Δ^{199}Hg; −0.22 to −0.01 ‰, Demers et al., 2013; Gratz et al., 2010; Sherman et al., 2010), and sites influenced by TGM evaded from the coastal surface (Δ^{200}Hg; −0.19 to −0.06 ‰, Δ^{199}Hg; −0.41 to −0.03 ‰, Rolison et al., 2013), rice paddy soil (Δ^{200}Hg; −0.07 to 0.03 ‰, Δ^{199}Hg; −0.34 to −0.24 ‰, Yin et al., 2013), and snowpack (Δ^{200}Hg; −0.22 to 0.02 ‰, Δ^{199}Hg; −0.46 to −0.10 ‰, Araujo et al., 2022).

3.3. Sources and processes affecting PBM

Unlike the TGM, the minor seasonal trend in PBM isotope ratios and the significant positive relationship between Δ^{199}Hg and 1/THg of PBM (r^2 = 0.39, $p < 0.05$) (Fig. 5A), with few exceptions in winter and summer (discussed below), imply that the sources of PBM may be more consistent across season. It is thought that PBM is generally originated from direct anthropogenic emissions and/or gas-particle partitioning of Hg^{2+} (Amos et al., 2012; Shah et al., 2021). To evaluate the importance of local anthropogenic emissions as the major PBM source, we compare our daily PBM concentrations to total Fe concentrations measured in the particles and PM_{10} acquired from the air quality monitoring station, both of which are known to be emitted from the local steel manufacturing industry (Fig. A.3.). While the PM_{10} and Fe concentrations match well temporally (r^2 = 0.57, $p < 0.05$), the PBM display absence of temporal relationships with the PM_{10} and Fe (r^2 = 0.00, r^2 = 0.03, both $p > 0.05$). This indicates that our PBM may not be derived from the same local anthropogenic source as the PM_{10} and Fe. Alternatively, our PBM may be subjected to further atmospheric processing, which modifies PBM concentration upon emission.

The importance of local anthropogenic emissions sourcing PBM is verified by the Δ^{199}Hg and 1/THg relationship, which reveals a gradual dilution of PBM concentration with increasing Δ^{199}Hg away from the anthropogenic PBM end-member (−0.04 ‰) (R. Sun et al., 2016) (Fig. 5A). The atmospheric process resulting in a higher Δ^{199}Hg together with a reduction in PBM concentration would be the Hg^{2+} photo-reduction on particles, given that measurable MIF occurs primarily via Hg^{2+} photo-reduction and MeHg photo-degradation (Bergquist and Blum, 2007). The importance of photo-reduction modifying our PBM isotope ratios is further confirmed by comparing our results with PBM characterized along coastal and offshore regions of the Northwest Pacific (Huang et al., 2022). In that study, Huang et al. (2022) observed wide ranges in Δ^{199}Hg (−0.50 to 0.67 ‰) and Δ^{200}Hg (−0.11 to 0.42 ‰) and suggested that anthropogenically emitted PBM from East Asia are processed at the regional atmosphere via 1) Hg^{2+} photo-reduction, 2) Hg^0 oxidation, and 3) high tropospheric Hg^0 photo-oxidation followed by particle adsorption (Huang et al., 2022). As illustrated in Fig. 6, Hg^{2+} photo-reduction and Hg^0 oxidation followed by particle adsorption drive Δ^{199}Hg to positive and negative values, respectively. For Δ^{200}Hg, Hg^0 photo-oxidation is

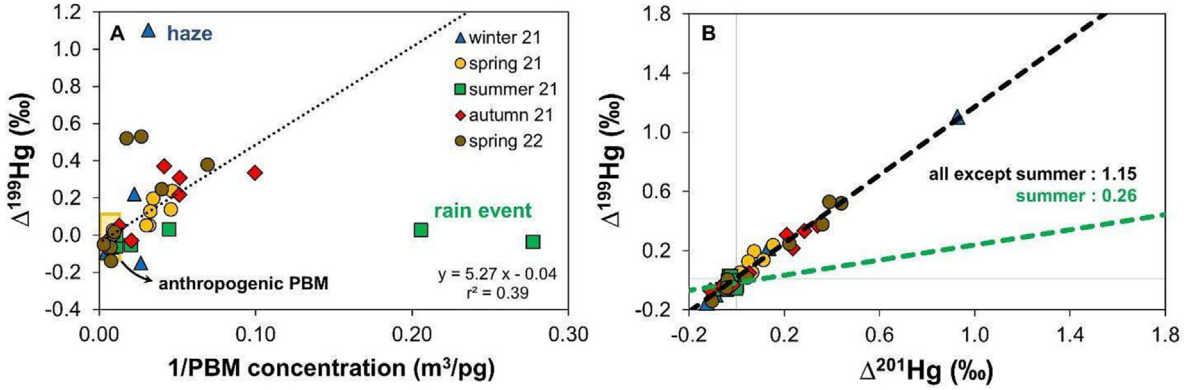

Fig. 5. (A) Δ^{199}Hg and total Hg concentrations of PBM (expressed in 1/THg of PBM). Yellow box represents the range of anthropogenic PBM Δ^{199}Hg end-member modeled by R. Sun et al. (2016). The linear regression excludes three data points labelled as haze and rain event. (B) Δ^{199}Hg and Δ^{201}Hg slopes of all PBM except summer (black dashed line) and of summer (green dashed line) measured in this study.

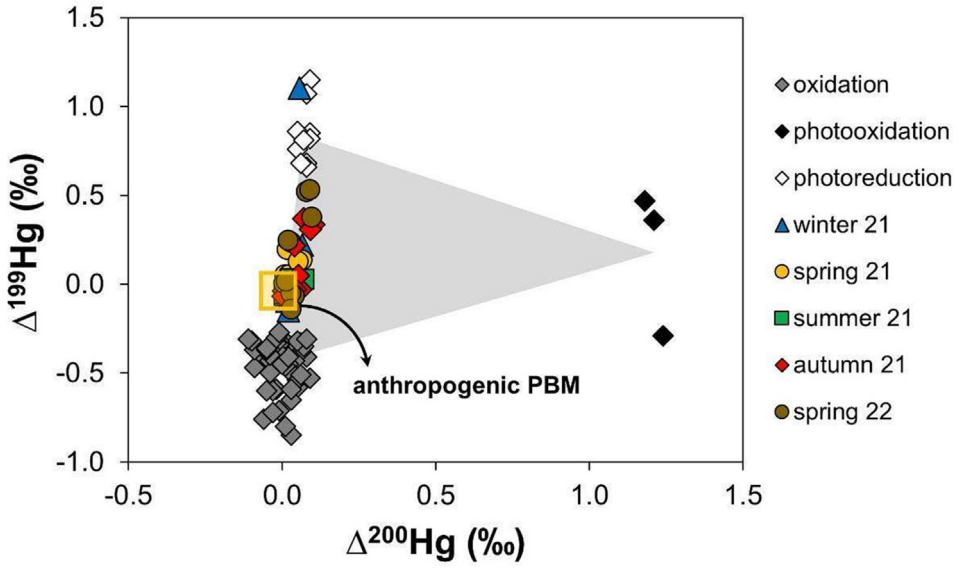

Fig. 6. Δ^{200}Hg and Δ^{199}Hg of the seasonal PBM. Yellow box represents the range of anthropogenic PBM Δ^{200}Hg and Δ^{199}Hg end-member modeled by R. Sun et al. (2016). Three end-members of atmospheric processes, established by Huang et al. (2022), are shown in white (Hg^{2+} photo-reduction), gray (Hg^0 oxidation), and black diamonds (Hg^0 photo-oxidation).

regarded as one of the dominant mechanisms altering Δ^{200}Hg in environmental samples (Cai and Chen, 2016). The fact that our PBM are situated between the anthropogenic PBM end-member, modeled by R. Sun et al. (2016), and PBM altered by photo-reduction indicate that Hg^{2+} photo-reduction is the dominant mechanism modifying locally emitted PBM at our sampling location.

Photo-reduction of Hg^{2+} on particles is thought to be particularly active in the coastal atmosphere characterized by high relative humidity and atmospheric moisture (Huang et al., 2022). A recent experimental study of Hg^{2+} photo-reduction on dry and aqueous soot particles has also reported increasing Δ^{199}Hg in Hg^{2+} in the aqueous phase but not in the dry phase, suggesting that aerosol water content determines the magnitude of photo-reduction and Δ^{199}Hg in PBM (Huang et al., 2021). As for Hg^0 oxidation, while Hg^0 evaded and transported from the coastal and land surface (as discussed in Section 3.2) may be subjected to oxidation in the local atmosphere prior to binding with particles, we observe no significant relationships between the Δ^{199}Hg of PBM and major oxidants (O_3, NO_2, CO, SO_2), obtained from the air quality monitoring station (Fig. A.4.). Moreover, the absence of a significant relationship between the Δ^{200}Hg and Δ^{204}Hg ($r^2 = 0.22$, $p > 0.05$), used to infer Hg^0 photo-oxidation (Cai and Chen, 2016), suggest that high tropospheric photo-oxidation is unlikely to supply Hg^{2+} to our PBM.

As noted previously, one PBM measured in winter display an anomalously high Δ^{199}Hg and few PBM collected in summer exhibit low concentrations (Fig. 5A). To first explain the low PBM concentrations in summer, note that these PBM were sampled on the days of the heaviest rainfall (14–51 mm; Table A.1.), but the total particle weights were similar to that of other sampling periods. We think that wet scavenging of atmospheric Hg species has suppressed Hg^0 oxidation and/or gas-particle partitioning of Hg^{2+}, resulting in exceptionally low concentrations. The elevated Δ^{199}Hg in the winter PBM corresponds with PBM collected during haze events in the wintertime over China (Qiu et al., 2022; Zhang et al., 2022) (Fig. 2B). Zhang et al. (2022) observed a significant positive relationship between Δ^{199}Hg and the concentration of humic acid-like water-soluble organic carbon in PBM, which constitutes the largest number of organic species during haze episodes. In that same study, experiments of Hg^{2+} photo-reduction in the presence of water-soluble organic carbon revealed up to 4 ‰ of Δ^{199}Hg in Hg^{2+}, implying that the physicochemical properties of PBM determine the extent of Hg^{2+} photo-reduction on particles.

Given the absence of significant inter-seasonal variability in PBM isotope ratios, we presume that seasonal meteorology and environmental factors play minor roles in governing sources and processes affecting PBM. Using the slope of Δ^{199}Hg/Δ^{201}Hg, we attempt to gain insights into the extent and/or mechanisms driving Hg^{2+} photo-reduction on particles in PBM. The Δ^{199}Hg/Δ^{201}Hg slope has been used to decipher between Hg^{2+} photo-reduction (~1.0) and MeHg photo-degradation (~1.3) (Bergquist and Blum, 2007), and Hg^{2+} photo-reduction occurring in the presence of variable ligand types (Motta et al., 2020; Zhang et al., 2022; Zhao et al., 2021; Zheng and Hintelmann, 2010). Our PBM reveal a relative consistent slope of 1.15, except for summer, which exhibits a depleted slope of ~0.26 (Fig. 5B). The depleted Δ^{199}Hg/Δ^{201}Hg slope likely reflect anthropogenically emitted PBM, which have undergone little atmospheric processing. This is verified by the overlapping isotope ratios between our summer PBM and PBM characterized at urban sites of China (Fig. 2B). The remaining PBM display Δ^{199}Hg/Δ^{201}Hg slopes that are higher than those derived from experimental Hg^{2+} photo-reduction in the presence of dissolved organic carbon (DOC) (~1.0) (Bergquist and Blum, 2007). We speculate that different physicochemical properties or ligand type present in PBM may explain the higher Δ^{199}Hg/Δ^{201}Hg. In particular, Hg^{2+} photo-reduction in the presence of O-containing ligands (i.e., oxalates), supplied by atmospheric oxidation processes, has shown a higher Δ^{199}Hg/ Δ^{201}Hg of 1.19 (Zhao et al., 2021), which matches well with our PBM. We suggest that additional experiments and detailed characterization are needed to identify precisely physicochemical properties driving photo-reduction and PBM isotope ratios.

4. Conclusion

The characterization of concentration and isotope ratios of TGM and PBM provide in-depth insights into sources and processes affecting two atmospheric Hg species in a coastal city of South Korea. We find that Hg^0 evaded from the coastal surface and those evaded and transported from long distances from high latitude regions act as important TGM sources relative to the local anthropogenic activities in Pohang. Conversely, the PBM are mostly sourced from local anthropogenic emissions, which is then subjected to Hg^{2+} photo-reduction on particles from the regional atmosphere. The type and the extent of Hg^{2+} photo-reduction may be dependent on the presence atmospheric ligands, which govern the PBM isotope ratios. From a local Hg management perspective, the implementation of effective air

pollution control device would lead to direct abatement of local anthropogenic PBM emissions. As for the TGM, regional and/or multilateral effort is likely required to achieve overall reductions of atmospheric Hg entering the natural environment and subsequent Hg^0 evasions from the surface.

Another regional insight is the similarity of PBM isotope ratios between our sampling location and PBM collected at a coastal city of Daimeishan, China (Xu et al., 2021) and those sampled along coastal and offshore regions of the Northwest Pacific (Huang et al., 2022). These results collectively imply that PBM sourced anthropogenically from East Asia and processed photochemically in the coastal atmosphere, resulting in characteristically positive δ^{202}Hg and Δ^{199}Hg in PBM, serve as key sources and processes that generate regional PBM isotopic end-member. Unlike the prior studies, which have repeatedly characterized PBM isotope ratios at inland urban and remote sites (Das et al., 2016; Guo et al., 2022; Huang et al., 2016, 2018; Xu et al., 2017), we expect that the regional isotopic end-member can be used to quantify the relative influence of local anthropogenic Hg emissions versus complex processes affecting PBM in East Asia and other geographical regions surrounded by coastal oceans.

CRediT authorship contribution statement

Hoin Lee: Investigation, Formal analysis, Visualization, Writing – original draft. **Sae Yun Kwon:** Conceptualization, Resources, Funding acquisition, Writing – review & editing, Supervision. **Jonghun Kam:** Funding acquisition, Validation, Writing – review & editing. **Kitack Lee:** Funding acquisition, Validation, Writing – review & editing. **Xuewu Fu:** Validation, Writing – review & editing. **In-Gyu Cho:** Validation, Writing – review & editing. **Sung-Deuk Choi:** Validation, Writing – review & editing.

Data availability

Data available within the supplementary material.

Declaration of competing interest

The authors declare that they have no known competing financial interests or personal relationships that could have appeared to influence the work reported in this paper.

Acknowledgements

This work was supported by the National Research Foundation of Korea (NRF) funded by the Korea government (MSIT) (NRF-2020R1A4A1018818), and Korea Institute of Marine Science & Technology Promotion (KIMST) funded by the Ministry of Oceans and Fisheries, Korea (20220534).

Appendix A. Supplementary data

Supplementary data to this article can be found online at https://doi.org/10.1016/j.scitotenv.2023.164404.

References

Amos, H.M., Jacob, D.J., Holmes, C.D., Fisher, J.A., Wang, Q., Yantosca, R.M., ... Sunderland, E.M., 2012. Gas-particle partitioning of atmospheric Hg (II) and its effect on global mercury deposition. Atmos. Chem. Phys. 12 (1), 591–603. https://doi.org/10.5194/acp-12-591-2012.

Araujo, B.F., Osterwalder, S., Szponar, N., Lee, D., Petrova, M.V., Pernov, J.B., ... Sonke, J.E., 2022. Mercury isotope evidence for Arctic summertime re-emission of mercury from the cryosphere. Nat. Commun. 13 (1), 4956. https://doi.org/10.1038/s41467-022-32440-8.

Baek, K.M., Kim, M.J., Kim, J.Y., Seo, Y.K., Baek, S.O., 2020. Characterization and health impact assessment of hazardous air pollutants in residential areas near a large iron-steel industrial complex in Korea. Atmos. Pollut. Res. 11 (10), 1754–1766. https://doi.org/10.1016/j.apr.2020.07.009.

Bergquist, B.A., Blum, J.D., 2007. Mass-dependent and-independent fractionation of hg isotopes by photoreduction in aquatic systems. Science 318 (5849), 417–420. https://doi.org/10.1126/science.1148050.

Blum, J.D., Sherman, L.S., Johnson, M.W., 2014. Mercury isotopes in earth and environmental sciences. Annu. Rev. Earth Planet. Sci. 42, 249–269. https://doi.org/10.1146/annurev-earth-050212-124107.

Butler, T.J., Cohen, M.D., Vermeylen, F.M., Likens, G.E., Schmeltz, D., Artz, R.S., 2008. Regional precipitation mercury trends in the eastern USA, 1998–2005: declines in the Northeast and Midwest, no trend in the Southeast. Atmos. Environ. 42 (7), 1582–1592. https://doi.org/10.1016/j.atmosenv.2007.10.084.

Cai, H., Chen, J., 2016. Mass-independent fractionation of even mercury isotopes. Sci. Bull. 61 (2), 116–124. https://doi.org/10.1007/s11434-015-0968-8.

Cole, A.S., Steffen, A., Pfaffhuber, K.A., Berg, T., Pilote, M., Poissant, L., ... Hung, H., 2013. Ten-year trends of atmospheric mercury in the high Arctic compared to Canadian sub-Arctic and mid-latitude sites. Atmos. Chem. Phys. 13 (3), 1535–1545. https://doi.org/10.5194/acp-13-1535-2013.

Das, R., Wang, X., Khezri, B., Webster, R.D., Sikdar, P.K., Datta, S., 2016. Mercury isotopes of atmospheric particle bound mercury for source apportionment study in urban Kolkata, IndiaMercury isotopes of atmospheric particle bound mercury. Elementa: Sci. the Anthrop. 4. https://doi.org/10.12952/journal.elementa.000098.

Demers, J.D., Blum, J.D., Zak, D.R., 2013. Mercury isotopes in a forested ecosystem: implications for air-surface exchange dynamics and the global mercury cycle. Glob. Biogeochem. Cycles 27 (1), 222–238. https://doi.org/10.1002/gbc.20021.

Demers, J.D., Sherman, L.S., Blum, J.D., Marsik, F.J., Dvonch, J.T., 2015. Coupling atmospheric mercury isotope ratios and meteorology to identify sources of mercury impacting a coastal urban-industrial region near Pensacola, Florida, USA. Glob. Biogeochem. Cycles 29 (10), 1689–1705. https://doi.org/10.1002/2015GB005146.

Draxler, R.R., Hess, G.D., 1998. An overview of the HYSPLIT_4 modelling system for trajectories. Aust. Meteorol. Mag. 47 (4), 295–308.

Driscoll, C.T., Mason, R.P., Chan, H.M., Jacob, D.J., Pirrone, N., 2013. Mercury as a global pollutant: sources, pathways, and effects. Environ. Sci. Technol. 47 (10), 4967–4983. https://doi.org/10.1021/es305071v.

Fu, X., Yang, X., Tan, Q., Ming, L., Lin, T., Lin, C.J., ... Feng, X., 2018. Isotopic composition of gaseous elemental mercury in the marine boundary layer of East China Sea. J. Geophys. Res. Atmos. 123 (14), 7656–7669. https://doi.org/10.1029/2018JD028671.

Fu, X., Zhang, H., Liu, C., Zhang, H., Lin, C.J., Feng, X., 2019. Significant seasonal variations in isotopic composition of atmospheric total gaseous mercury at forest sites in China caused by vegetation and mercury sources. Environ. Sci. Technol. 53 (23), 13748–13756. https://doi.org/10.1021/acs.est.9b05016.

Fu, X., Liu, C., Zhang, H., Xu, Y., Li, J., Lyu, X., ... Feng, X., 2021. Isotopic compositions of atmospheric total gaseous mercury in 10 Chinese cities and implications for land surface emissions. Atmos. Chem. Phys. 21 (9), 6721–6734. https://doi.org/10.5194/acp-21-6721-2021.

Gratz, L.E., Keeler, G.J., Blum, J.D., Sherman, L.S., 2010. Isotopic composition and fractionation of mercury in Great Lakes precipitation and ambient air. Environ. Sci. Technol. 44 (20), 7764–7770. https://doi.org/10.1021/es100383w.

Guo, J., Tripathee, L., Kang, S., Zhang, Q., Huang, J., Sharma, C.M., ... Rupakheti, D., 2022. Atmospheric particle-bound mercury in the northern Indo-Gangetic Plain region: insights into sources from mercury isotope analysis and influencing factors. Geosci. Front. 13 (1), 101274. https://doi.org/10.1016/j.gsf.2021.101274.

Hleis, D., Fernández-Olmo, I., Ledoux, F., Kfoury, A., Courcot, L., Desmonts, T., Courcot, D., 2013. Chemical profile identification of fugitive and confined particle emissions from an integrated iron and steelmaking plant. J. Hazard. Mater. 250, 246–255. https://doi.org/10.1016/j.jhazmat.2013.01.080.

Huang, Q., Liu, Y., Chen, J., Feng, X., Huang, W., Yuan, S., ... Fu, X., 2015. An improved dual-stage protocol to pre-concentrate mercury from airborne particles for precise isotopic measurement. J. Anal. At. Spectrom. 30 (4), 957–966. https://doi.org/10.1039/C4JA00438H.

Huang, Q., Chen, J., Huang, W., Fu, P., Guinot, B., Feng, X., ... Yu, B., 2016. Isotopic composition for source identification of mercury in atmospheric fine particles. Atmos. Chem. Phys. 16 (18), 11773–11786. https://doi.org/10.5194/acp-16-11773-2016.

Huang, Q., Chen, J., Huang, W., Reinfelder, J.R., Fu, P., Yuan, S., ... He, L., 2019. Diel variation in mercury stable isotope ratios records photoreduction of PM 2.5-bound mercury. Atmos. Chem. Phys. 19 (1), 315–325. https://doi.org/10.5194/acp-19-315-2019.

Huang, Q., He, X., Huang, W., Reinfelder, J.R., 2021. Mass-independent fractionation of mercury isotopes during photoreduction of soot particle bound Hg (II). Environ. Sci. Technol. 55 (20), 13783–13791. https://doi.org/10.1021/acs.est.1c02679.

Huang, S., Sun, L., Zhou, T., Yuan, D., Du, B., Sun, X., 2018. Natural stable isotopic compositions of mercury in aerosols and wet precipitations around a coal-fired power plant in Xiamen, Southeast China. Atmos. Environ. 173, 72–80. https://doi.org/10.1016/j.atmosenv.2017.11.003.

Huang, S., Huo, Y., Sun, H., Lv, S., Zhao, Y., Lin, K., … & Zhang, Y. (2022). Evidence for mass independent fractionation of even mercury isotopes in the troposphere. Atmos. Chem. Phys. Discuss., 1–42. Preprint. https://doi.org/10.5194/acp-2022-284.

Jiskra, M., Heimbürger-Boavida, L.E., Desgranges, M.M., Petrova, M.V., Dufour, A., Ferreira-Araujo, B., ... Sonke, J.E., 2021. Mercury stable isotopes constrain atmospheric sources to the ocean. Nature 597 (7878), 678–682. https://doi.org/10.1038/s41586-021-03859-8.

Jung, S., Kwon, S.Y., Hong, Y., Yin, R., Motta, L.C., 2021. Isotope investigation of mercury sources in a creek impacted by multiple anthropogenic activities. Chemosphere 282, 130947. https://doi.org/10.1016/j.chemosphere.2021.130947.

Kurisu, M., Adachi, K., Sakata, K., Takahashi, Y., 2019. Stable isotope ratios of combustion iron produced by evaporation in a steel plant. ACS Earth Space Chem. 3 (4), 588–598. https://doi.org/10.1021/acsearthspacechem.8b00171.

Kwon, S.Y., Selin, N.E., 2016. Uncertainties in atmospheric mercury modeling for policy evaluation. Curr. Pollut. Rep. 2 (2), 103–114. https://doi.org/10.1007/s40726-016-0030-8.

Kwon, S.Y., Blum, J.D., Yin, R., Tsui, M.T.K., Yang, Y.H., Choi, J.W., 2020. Mercury stable isotopes for monitoring the effectiveness of the Minamata Convention on Mercury. Earth Sci. Rev. 203, 103111. https://doi.org/10.1016/j.earscirev.2020.103111.

Li, C., Chen, J., Angot, H., Zheng, W., Shi, G., Ding, M., ... Qin, D., 2020. Seasonal variation of mercury and its isotopes in atmospheric particles at the coastal Zhongshan Station, Eastern Antarctica. Environ. Sci. Technol. 54 (18), 11344–11355. https://doi.org/10.1021/acs.est.0c04462.

Mergler, D., Anderson, H.A., Chan, L.H.M., Mahaffey, K.R., Murray, M., Sakamoto, M., Stern, A.H., 2007. Methylmercury exposure and health effects in humans: a worldwide concern. AMBIO J. Hum. Environ. 36 (1), 3–11. https://doi.org/10.1579/0044-7447(2007)36[3:MEAHEI]2.0.CO;2.

Motta, L.C., Blum, J.D., Johnson, M.W., Umhau, B.P., Popp, B.N., Washburn, S.J., ... Lamborg, C.H., 2019. Mercury cycling in the North Pacific Subtropical Gyre as revealed by mercury stable isotope ratios. Glob. Biogeochem. Cycles 33 (6), 777–794. https://doi.org/10.1029/2018GB006057.

Motta, L.C., Kritee, K., Blum, J.D., Tsz-Ki Tsui, M., Reinfelder, J.R., 2020. Mercury isotope fractionation during the photochemical reduction of Hg (II) coordinated with organic ligands. J. Phys. Chem. A 124 (14), 2842–2853. https://doi.org/10.1021/acs.jpca.9b06308.

Qiu, Y., Gai, P., Yue, F., Zhang, Y., He, P., Kang, H., ... Xie, Z., 2021. Stable mercury isotopes revealing photochemical processes in the marine boundary layer. J. Geophys. Res. Atmos. 126 (16), e2021JD034630. https://doi.org/10.1029/2021JD034630.

Qiu, Y., Gai, P., Yue, F., Zhang, Y., He, P., Kang, H., ... Xie, Z., 2022. Potential factors impacting PM2. 5-Hg during haze evolution revealed by mercury isotope: emission sources and photochemical processes. Atmos. Res. 277, 106318. https://doi.org/10.1016/j.atmosres.2022.106318.

Rolison, J.M., Landing, W.M., Luke, W., Cohen, M., Salters, V.J.M., 2013. Isotopic composition of species-specific atmospheric hg in a coastal environment. Chem. Geol. 336, 37–49. https://doi.org/10.1016/j.chemgeo.2012.10.007.

Sakata, K., Kurisu, M., Tanimoto, H., Sakaguchi, A., Uematsu, M., Miyamoto, C., Takahashi, Y., 2018. Custom-made PTFE filters for ultra-clean size-fractionated aerosol sampling for trace metals. Mar. Chem. 206, 100–108. https://doi.org/10.1016/j.marchem.2018.09.009.

Selin, N.E., 2009. Global biogeochemical cycling of mercury: a review. Annu. Rev. Environ. Resour. 34 (1), 43–63. https://doi.org/10.1146/annurev.environ.051308.084314.

Seo, Y.S., Jeong, S.P., Holsen, T.M., Han, Y.J., Choi, E., Park, E.H., ... Yi, S.M., 2016. Characteristics of total gaseous mercury (TGM) concentrations in an industrial complex in South Korea: impacts from local sources. Atmos. Chem. Phys. 16 (15), 10215–10228. https://doi.org/10.5194/acp-16-10215-2016.

Shah, V., Jacob, D.J., Thackray, C.P., Wang, X., Sunderland, E.M., Dibble, T.S., ... Wang, C., 2021. Improved mechanistic model of the atmospheric redox chemistry of mercury. Environ. Sci. Technol. 55 (21), 14445–14456. https://doi.org/10.1021/acs.est.1c03160.

Sherman, L.S., Blum, J.D., Johnson, K.P., Keeler, G.J., Barres, J.A., Douglas, T.A., 2010. Mass-independent fractionation of mercury isotopes in Arctic snow driven by sunlight. Nat. Geosci. 3 (3), 173–177. https://doi.org/10.1038/ngeo758.

Shi, J., Chen, Y., Xu, L., Hong, Y., Li, M., Fan, X., ... Chen, J., 2022. Measurement report: atmospheric mercury in a coastal city of Southeast China–inter-annual variations and influencing factors. Atmos. Chem. Phys. 22 (17), 11187–11202. https://doi.org/10.5194/acp-22-11187-2022.

Shin, D., Song, S., Ryoo, S.B., Lee, S.S., 2020. Variations in ozone concentration over the mid-latitude region revealed by ozonesonde observations in Pohang, South Korea. Atmosphere 11 (7), 746. https://doi.org/10.3390/atmos11070746.

Slemr, F., Brunke, E.G., Ebinghaus, R., Kuss, J., 2011. Worldwide trend of atmospheric mercury since 1995. Atmos. Chem. Phys. 11 (10), 4779–4787. https://doi.org/10.5194/acp-11-4779-2011.

Soerensen, A.L., Jacob, D.J., Streets, D.G., Witt, M.L., Ebinghaus, R., Mason, R.P., ... Sunderland, E.M., 2012. Multi-decadal decline of mercury in the North Atlantic atmosphere explained by changing subsurface seawater concentrations. Geophys. Res. Lett. 39 (21). https://doi.org/10.1029/2012GL053736.

Sonke, J.E., 2011. A global model of mass independent mercury stable isotope fractionation. Geochim. Cosmochim. Acta 75 (16), 4577–4590. https://doi.org/10.1016/j.gca.2011.05.027.

Streets, D.G., Horowitz, H.M., Jacob, D.J., Lu, Z., Levin, L., Ter Schure, A.F., Sunderland, E.M., 2017. Total mercury released to the environment by human activities. Environ. Sci. Technol. 51 (11), 5969–5977. https://doi.org/10.1021/acs.est.7b00451.

Streets, D.G., Horowitz, H.M., Lu, Z., Levin, L., Thackray, C.P., Sunderland, E.M., 2019. Global and regional trends in mercury emissions and concentrations, 2010–2015. Atmos. Environ. 201, 417–427. https://doi.org/10.1016/j.atmosenv.2018.12.031.

Sun, G., Feng, X., Yin, R., Wang, F., Lin, C.J., Li, K., Sommar, J.O., 2022. Dissociation of mercuric oxides drives anomalous isotope fractionation during net photo-oxidation of mercury vapor in air. Environ. Sci. Technol. 56 (18), 13428–13438. https://doi.org/10.1021/acs.est.2c02722.

Sun, R., Streets, D.G., Horowitz, H.M., Amos, H.M., Liu, G., Perrot, V., ... Sonke, J.E., 2016. Historical (1850–2010) mercury stable isotope inventory from anthropogenic sources to the atmosphereMercury isotope emission inventory. Elementa: Sci. the Anthrop. 4. https://doi.org/10.12952/journal.elementa.000091.

Sun, R., Jiskra, M., Amos, H.M., Zhang, Y., Sunderland, E.M., Sonke, J.E., 2019. Modelling the mercury stable isotope distribution of Earth surface reservoirs: implications for global Hg cycling. Geochim. Cosmochim. Acta 246, 156–173. https://doi.org/10.1016/j.gca.2018.11.036.

Tang, L., Xue, X., Jia, M., Jing, H., Wang, T., Zhen, R., ... Wang, S., 2020. Iron and steel industry emissions and contribution to the air quality in China. Atmos. Environ. 237, 117668. https://doi.org/10.1016/j.atmosenv.2020.117668.

UNEP, 2019. Global Mercury Assessment 2018. UNEP-UN Environment Programme.

Xu, H., Sonke, J.E., Guinot, B., Fu, X., Sun, R., Lanzanova, A., ... Cao, J., 2017. Seasonal and annual variations in atmospheric Hg and Pb isotopes in Xi'an, China. Environ. Sci. Technol. 51 (7), 3759–3766. https://doi.org/10.1021/acs.est.6b06145.

Xu, H.M., Sun, R.Y., Cao, J.J., Huang, R.J., Guinot, B., Shen, Z.X., ... Sonke, J.E., 2019. Mercury stable isotope compositions of Chinese urban fine particulates in winter haze days: implications for Hg sources and transformations. Chem. Geol. 504, 267–275. https://doi.org/10.1016/j.chemgeo.2018.11.018.

Xu, L., Shi, J., Chen, Y., Zhang, Y., Yang, M., Chen, Y., ... Chen, J., 2021. Mercury isotopic compositions in fine particles and offshore surface seawater in a coastal area of East China: implications for Hg sources and atmospheric transformations. Atmos. Chem. Phys. 21 (24), 18543–18555. https://doi.org/10.5194/acp-21-18543-2021.

Yin, R., Feng, X., Meng, B., 2013. Stable mercury isotope variation in rice plants (Oryza sativa L.) from the Wanshan mercury mining district, SW China. Environ. Sci. Technol. 47 (5), 2238–2245. https://doi.org/10.1021/es304302a.

Yu, B., Fu, X., Yin, R., Zhang, H., Wang, X., Lin, C.J., ... Feng, X., 2016. Isotopic composition of atmospheric mercury in China: new evidence for sources and transformation processes in air and in vegetation. Environ. Sci. Technol. 50 (17), 9262–9269. https://doi.org/10.1021/acs.est.6b01782.

Zhang, K., Zheng, W., Sun, R., He, S., Shuai, W., Fan, X., ... Chen, J., 2022. Stable isotopes reveal photoreduction of particle-bound mercury driven by water-soluble organic carbon during severe haze. Environ. Sci. Technol. 56 (15), 10619–10628. https://doi.org/10.1021/acs.est.2c01933.

Zhang, Y., Jacob, D.J., Horowitz, H.M., Chen, L., Amos, H.M., Krabbenhoft, D.P., ... Sunderland, E.M., 2016. Observed decrease in atmospheric mercury explained by global decline in anthropogenic emissions. Proc. Natl. Acad. Sci. 113 (3), 526–531. https://doi.org/10.1073/pnas.1516312113.

Zhao, H., Meng, B., Sun, G., Lin, C.J., Feng, X., Sommar, J., 2021. Chemistry and isotope fractionation of divalent mercury during aqueous reduction mediated by selected oxygenated organic ligands. Environ. Sci. Technol. 55 (19), 13376–13386. https://doi.org/10.1021/acs.est.1c03171.

Zheng, W., Hintelmann, H., 2010. Isotope fractionation of mercury during its photochemical reduction by low-molecular-weight organic compounds. J. Phys. Chem. A 114 (12), 4246–4253. https://doi.org/10.1021/jp9111348.

Zhu, Y., Li, W., Wang, Y., Zhang, J., Liu, L., Xu, L., ... Shi, Z., 2022. Sources and processes of iron aerosols in a megacity in eastern China. Atmos. Chem. Phys. 22 (4), 2191–2202. https://doi.org/10.5194/acp-22-2191-2022.